Geophysical Journal International

Geophys. J. Int. (2011) **185**, 1090-1102 doi: 10.1111/j.1365-246X.2011.04992.x

Geomechanical model of the Marmara Sea region—II. 3-D contemporary background stress field

Tobias Hergert[1,*], and Oliver Heidbach[2]

[1] *Geophysical Institute, Karlsruhe Institute of Technology (KIT), Hertzstr. 16, 76187 Karlsruhe, Germany. E-mail: tobias.hergert@gpi.uni-karlsruhe.de*
[2] *GFZ German Research Centre for Geosciences, Section 2.6 Seismic Hazard and Stress Field, Telegrafenberg, 14773 Potsdam, Germany*

Accepted 2011 February 17. Received 2010 February 10; in original form 2010 February 22

SUMMARY

We present the contemporary 3-D background stress field of the Marmara Sea region derived from a geomechanical model. The background stress field (i.e. the component of the absolute stress state that is time-independent over the seismic cycle) primarily depends on the distribution of density and elastic parameters, on the acting far-field stresses from plate boundary forces and on fault geometries. We take these into account to predict the 3-D background stress field including its spatial variations. Technically, our model concept involves the definition of an appropriate initial stress state accounting for the gravitational reference stress state of the crust, which is then changed by plate tectonics until the 3-D background stress field has evolved. The modelled stress field agrees well with observations from earthquake focal mechanism solutions and their formal stress inversion, with orientation of maximum horizontal stress and with the distribution of seismicity in the Marmara Sea. In particular in the vicinity of fault bends the stress field deviates considerably from the regional NW-SE oriented maximum horizontal stress and exhibits variability of the stress regime. Our model results are consistent not only with dynamic observations but also with kinematic ones. Various kinematic observations are understandable from the stress field. We show that a stress regime that indicates normal faulting in the basins is nonetheless reconcilable with almost pure strike-slip motion on the Main Marmara Fault. The distribution of seismicity in the Marmara Sea can be explained in first order by the distribution of critical differential stress, which is closely related to local fault geometries. We refer the wide absence of seismicity between the bend of the Main Marmara Fault near Istanbul and the Central basin to the relatively plane fault geometry of that segment. Normal stress on the Main Marmara Fault is highly variable along strike, which makes segment-wise rupture more likely than a rupture of the seismic gap at once. Comparably low normal stress on the Prince's Islands Segment indicates a shorter interevent time for this fault segment than for the central segment of the Main Marmara Fault.

Key words: Numerical solutions; Geomechanics; Transform faults; Dynamics: seismotectonics.

1 INTRODUCTION

In general, the absolute state of stress within a plate boundary region can be described as a superposition of two components that act on different temporal scales. The first component is what we call herein the background stress field that primarily originates (a) from the regional density distribution subjected to gravity, (b) from the far-field plate boundary forces such as ridge push, slab pull and collision of tectonic plates (*Zoback* 1992) and (c) from active faults as well as from local density and stiffness contrasts that cause perturbations of the regional stress field (*Heidbach et al.* 2007).

The background stress field can be assumed as time-independent within periods of several thousand years. The second component of the absolute stress state are stresses associated with the seismic cycle, that is, stress build-up at locked faults during the interseismic period, stress drop during an earthquake and post-seismic stress relaxation (*Lorenzo-Martin et al.* 2006; *Hearn et al.* 2009). Thus, in particular near seismically active faults the absolute stress field is time-dependent.

In the Marmara Sea region the time-dependent component of the absolute stress field has been quantified in terms of changes of Coulomb Failure Stress (ΔCFS) due to co-, inter- and post-seismic stress transfer to quantify seismic hazard (*Hubert-Ferrari et al.* 2000; *Parsons et al.* 2000; *Muller et al.* 2003, 2006; *Parsons* 2004; *Lorenzo-Martin et al.* 2006). The time-independent component, that is, the background stress field, has been used to calculate ΔCFS on optimally oriented planes (*Stein et al.* 1997; *Hubert-Ferrari et al.* 2000; *Lorenzo-Martin et al.* 2006) and to simulate dynamic rupture propagation (*Oglesby et al.* 2008). Commonly, the background stress field is approximated by a uniform orientation of the maximum horizontal stress (σ_H) and its magnitude. For the Main Marmara Fault (MMF) *Oglesby et al.* (2008) point out that rupture propagation crucially depends

*Now at: Landesforschungszentrum für Geothermie, Institute for Applied Geosciences, Karlsruhe Institute of Technology (KIT), Kaiserstraße 12, 76128 Karlsruhe, Germany.

on the adopted background stress field. In this respect, it is vital to quantify the non-uniform background stress field including its perturbations arising from the complex fault geometries and heterogeneities in rock properties beneath the Marmara Sea.

Our present knowledge of the contemporary background stress field in the Marmara Sea region comes from earthquake focal mechanisms and their formal stress inversion (*Eyidoğan* 1988; *Taymaz et al.* 1991; *Gürbüz et al.* 2000; *Örgülü & Aktar* 2001; *Karabulut et al.* 2002; *Kiratzi* 2002; *Özalaybey et al.* 2002; *Polat et al.* 2002a; *Pınar et al.* 2003; *Sato et al.* 2004; *Bohnhoff et al.* 2006; *Bulut & Aktar* 2007; *Bulut et al.* 2007). From these the σ_H orientation can be estimated as well as the tectonic regime (*Anderson* 1905; *Zoback* 1992). Data of the World Stress Map (WSM) database release 2008 (*Heidbach et al.* 2008b) show that the σ_H orientation in the greater Marmara Sea region rotates from NNW-SSE in the East over NW-SE in the Marmara Sea to E-W in the North Aegean Sea (Fig. 1a). This reflects that in this region two far-field stress sources are superimposed: (1) the indentation of the Arabian Plate into Eurasia and the consequent lateral extrusion of the Anatolian Plate along the North Anatolian Fault, and (2) the N-S directed backarc spreading in the broader Aegean due to the roll-back of the Hellenic arc subduction zone (*McKenzie* 1972; *Le Pichon & Angelier* 1979; *Taymaz et al.* 1991; *Heidbach & Drewes* 2003). In the Marmara Sea local variations of σ_H orientation and tectonic regime appear (Fig. 1b), which indicates that structural complexities also affect the stress field.

To obtain a spatially continuous 3-D background stress field instead of point-wise information of σ_H orientation and tectonic regime 3-D geomechanical modelling becomes effective. This requires consideration of sources of stress that are not needed when aiming at stress differences such as ΔCFS. So far, geomechanical models that fit stress observations are mainly 2.5 D approaches that solve the equations of equilibrium in 2-D and add the integrated effect of the vertical stress due to the given density distribution (*Provost et al.* 2003; *Bird et al.* 2006; *Ghosh et al.* 2006; *Flesch et al.* 2007; *Humphreys & Coblentz* 2007; *Heidbach et al.* 2008a; *Carena & Moder* 2009). However, the thin-plate approximation assumes as a prerequisite that lateral variations of stiffness and density are of larger wavelength than the thickness of the crust. This is not the case in the Marmara Sea region with its steep gradients in bathymetry, basement-topography and Moho (*Laigle et al.* 2008).

Here, we present a 3-D geomechanical model of the Marmara Sea region that solves the 3-D equations of equilibrium of forces. It incorporates the structural complexities and inhomogeneous rock property distribution to predict the 3-D contemporary background stress field and its spatial variations. An integral part of our approach to model the background stress field is to define an appropriate initial stress state in the model that represents a gravitational reference stress state of the crust, before we apply plate tectonic boundary conditions.

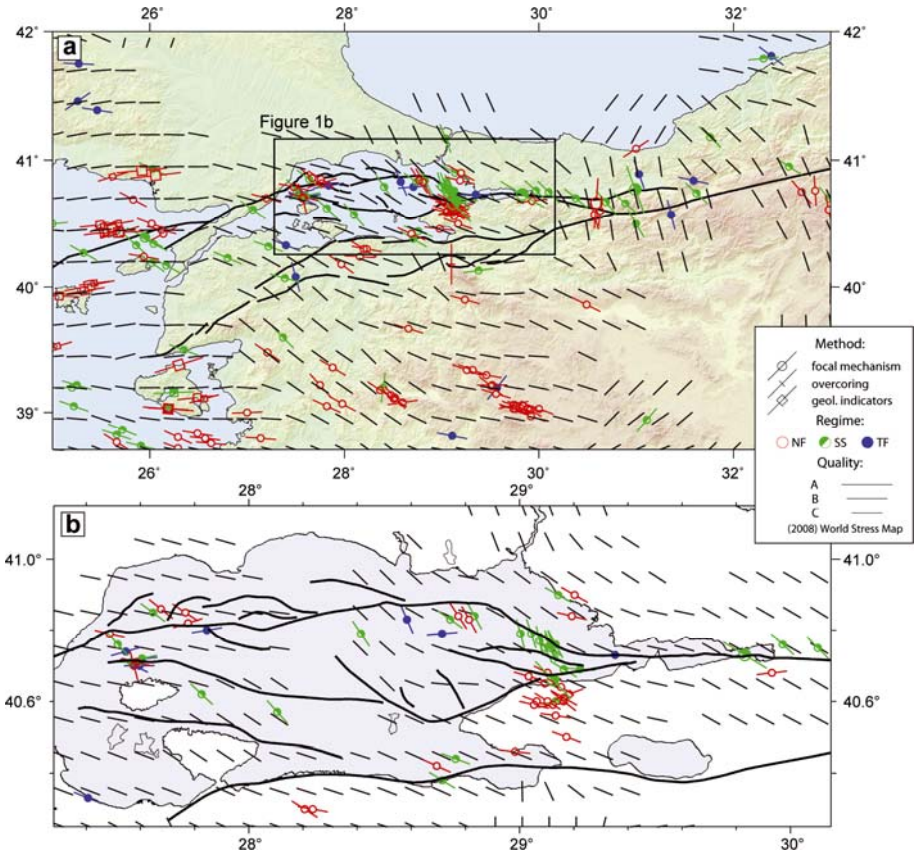

Figure 1. Stress maps based on data from the World Stress Map (WSM) database release 2008 (*Heidbach et al.* 2008b). Coloured lines show the orientation of maximum horizontal compressional stress (σ_H) with line length proportional to data quality. Red indicates normal faulting tectonic regime, green strike-slip and blue thrust faulting. Grey lines on a grid display mean σ_H orientation calculated with a quality- and distance-weighted smoothing algorithm (*Müller et al.* 2003; *Heidbach et al.* 2010). (a) NW Anatolia. Mean σ_H orientations are calculated using a search radius of 75 km. (b) Marmara Sea area. Mean σ_H orientations are calculated with a search radius of 25 km. Note, that the tectonic regime changes on short spatial scales indicating either that principal stresses are of similar magnitude or that local effects due to active faults and lateral density and stiffness contrasts change the stress field. (b) shows the area of our model.

The model set-up we use is exactly the same as described in *Hergert et al.* (2011, herein cited as Paper I). For details on the tectonic setting of the Marmara Sea region, the model geometry, rock properties and tectonic boundary conditions we refer to Paper I. If not stated otherwise, all results presented herein are from the model with MAT_lay rock property distribution (table 1 in Paper I) and an effective coefficient of friction of $\mu' = 0.05$ on all faults.

To validate the model, we compare the modelled stress field with model-independent stress data such as σ_H orientations, stress inversions of earthquake focal mechanisms, data reflecting the tectonic regime and the distribution of seismicity. We critically discuss our model limitations and uncertainties, but also outline the challenges and perspectives of our approach with respect to earthquake hazard assessment. In the following section, we present our approach for the definition of a 3-D initial stress state of the Marmara model.

2 INITIAL STRESS STATE

We model the contemporary background stress field in two steps. In the first step, we establish an initial stress state, which describes the state of stress in the absence of plate tectonic stresses. This initial stress state is based on an analytical description of the reference stress state of the crust (*McGarr* 1988; *Jaeger et al.* 2007; *Zang & Stephansson* 2010), which accounts for an appropriate ratio of the mean horizontal to vertical stress. In addition to the reference stress state, our implemented initial stress accounts for the inhomogeneous distribution of rock density and stiffness in the field of gravity. Thereafter in the second step, we apply kinematic boundary conditions that simulate the far-field stresses resulting from the plate boundary forces (Paper I).

Several analytical stress states have been proposed to describe the reference stress state of the crust. To evaluate these in the light of observations we first present a global compilation of stress magnitude measurements.

2.1 Compilation of stress magnitude measurements

Measurements of stress magnitudes in boreholes and mines are limited to the upper few kilometres of the crust. Fig. 2 shows a global compilation of the ratio k of the magnitude of mean horizontal stress $\sigma_{\bar{H}} = (\sigma_H + \sigma_h)/2$ to the magnitude of vertical stress σ_v (σ_H and σ_h are the maximum and minimum horizontal stress, respectively). The k-values are in the range from about 0.4 to over 3 and there is evidence for increasing k-values towards the surface.

All these stress measurements include both, the reference stress state and the tectonic stresses. This implies that in the compiled k-values the reference stress state is obscured by the tectonic stresses, which depending on the tectonic setting increase or decrease the k-value of the reference stress state. As an example, the k-value at the pilot borehole of the San Andreas Fault Observatory at Depth (SAFOD) is between 1.7 and 2.3 (*Hickman & Zoback* 2004), which is well above the values measured at other places (Fig. 2). Here the tectonic boundary conditions due to the transpressive plate boundary between the Pacific Plate and the North American Plate add to the horizontal stress of the reference stress state and increase the k-value. Conversely, the k-value in areas under extension is reduced with respect to the reference stress state. The data set comprises stress magnitudes from all tectonic regimes and the high-quality stress magnitude data from the Continental Deep Drilling Program (KTB; *Brudy et al.* 1997).

2.2 Analytical models of the reference stress state

A widely used description of the reference stress state results from the vertically downward acting force of gravity and the assumption of horizontal displacements constrained to zero

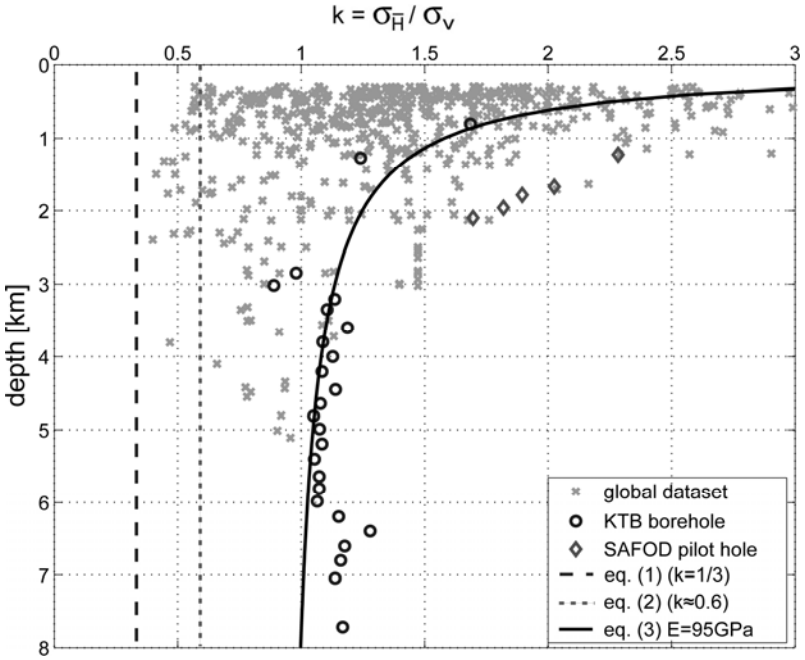

Figure 2. Global compilation of k-values ($k = \sigma_{\bar{H}}/\sigma_V$) from >300 m depth (for references see Supporting Information) including data from the KTB site (*Brudy et al.* 1997) and the SAFOD pilot hole (*Hickman & Zoback* 2004); details on the compilation are given in the Supporting Information. Dashed line shows k-values from Poisson's constraint for $\nu = 0.25$ (eq. 1). Dotted line shows the k-value in poroelastic rock for $\nu = 0.25$, hydrostatic pore pressure P_f, $\alpha = 1$ and $\rho = 2.65$ g cm^{-3} (eq. 2). Solid line shows eq. (3) for the Young's modulus measured at the KTB site.

(i.e. uniaxial strain condition). The magnitude of the vertical stress σ_V can be approximated by the weight of the overburden. For homogeneous and isotropic rock the mean horizontal compressional stress $\sigma_{\bar{H}}$ is then given by

$$\sigma_{\bar{H}} = \frac{\nu}{1-\nu}\sigma_{\mathrm{v}} = k\sigma_{\mathrm{v}} \quad (1)$$

with ν the Poisson's ratio (*Jaeger et al.* 2007). In poroelastic rock another term adds to the horizontal stress at uniaxial strain condition (*Engelder & Fischer* 1994)

$$\sigma_{\bar{H}} = \frac{\nu}{1-\nu}\sigma_{\mathrm{v}} + \alpha\frac{1-2\nu}{1-\nu}P_f \quad (2)$$

where P_f is pore fluid pressure and α the Biot coefficient of effective stress. With ν = 0.25, hydrostatic pore fluid pressure, density ρ = 2.65 g/cm^3 and α = 1 the value of k is ~0.6. Neglecting pore fluid pressure the k-value is 1/3 (from eq. (1)). However, Fig. 2 shows that the k-value of 1/3 is even lower than the values measured in areas under extension and it does not reflect the observed increase towards the surface. Therefore, this analytical stress state is in general not appropriate (*McGarr* 1988).

Another analytical description of the reference stress state was proposed by *Sheorey* (1994). For the uppermost kilometres of the crust *Sheorey* (1994) provides an approximation for the k-value

$$k = 0.25 + 7E(0.001 + 1/z), \quad (3)$$

where E is Young's modulus (GPa) and z depth (m). Regardless whether or not the physical grounds behind eq. (3) are justified, it delivers a good mathematical model to approximate the stress measurements. In particular the k-values measured at the KTB borehole are predicted very well when the measured Young's modulus at the KTB borehole of E = 95 GPa (*Brudy et al.* 1997) is used in eq. (3) (Fig. 2). Note that Sheorey's model was established before the KTB data were available.

2.3 Initial stress state in the Marmara Sea model

To define a reference stress state for our geomechanical model we make two assumptions: (1) The measured k-values at the KTB site are unaffected by tectonic loading and thus represent a reference stress state. (2) Eq. (3) represents a reasonable analytical description of the crustal reference stress state. We model our initial stress state such that the modelled k-values fit eq. (3), in which we insert the values of the Young's modulus from our model. Fig. 3 shows that the modelled initial stress state is satisfactorily established at three test sites, as the modelled k-values fit the reference state according to eq. (3). After this step, we apply the kinematic boundary conditions to account for tectonic loading.

3 STRESS ORIENTATIONS

In the following sections we present the results from the model MAT_lay, if not stated otherwise (table 1 in Paper I). We compare the modelled stress field with data of the orientation of maximum horizontal stress, principal stresses, stress regime and seismicity. Again, we would like to emphasize that the model set-up we use is exactly the same as described in Paper I; that is, the kinematic results presented in Paper I correspond to the stress state presented in the following.

3.1 Orientation of maximum horizontal stress σ_H

We calculate the σ_H orientation from the modelled stress field at 5 km bsl. using the definition of *Lund & Townend* (2007), thus taking all three principal stresses into account. σ_H is oriented basically NW-SE in the Marmara Sea region, but deviations from this regional orientation appear locally (Fig. 4a). Near the faults σ_H orientations are in part scattered due to the low coefficient of friction (μ' = 0.05) requiring either very low or high angles of σ_H orientation with respect to the local fault strike. However, WSM data confirm a NNW-SSE oriented σ_H northwest of the Çınarcık Basin and more or less EW oriented σ_H in the western Marmara Sea beneath the Western High, Tekirdağ Basin and to the south towards

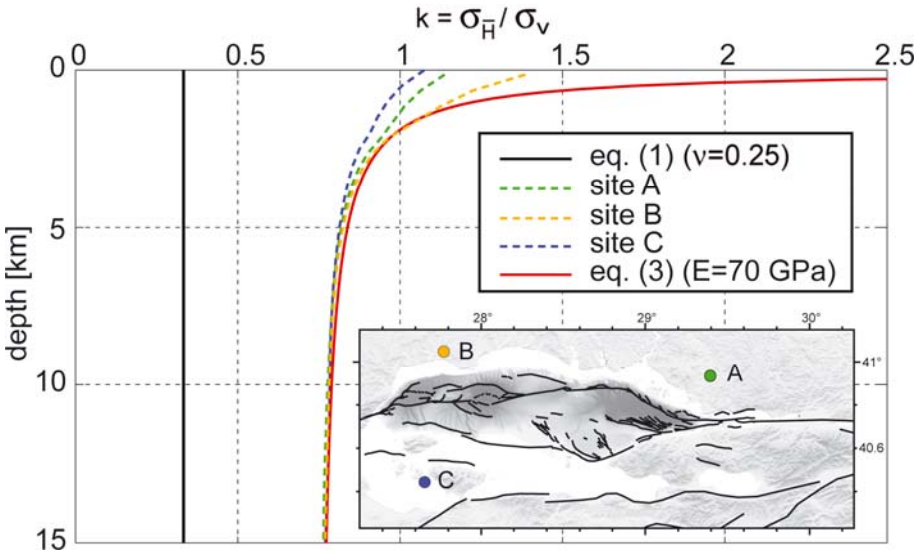

Figure 3. Depth profiles of the initial k-values (dashed lines) at three test sites indicated on the inset map. Solid red line shows the stress state given by eq. (3), which we consider as reference stress state. For comparison the low k-value from eq. (1) is also shown (black line).

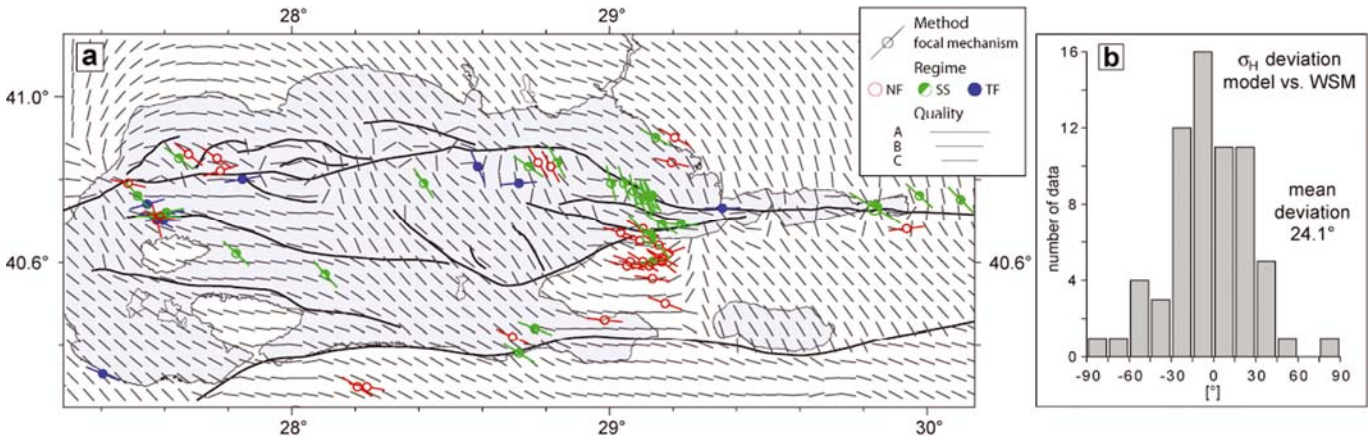

Figure 4. Modelled maximum horizontal stress orientations σ_H at 5 km bsl. extrapolated on a 0.05°E x 0.1°N grid (black lines). Coloured lines show the σ_H orientations of the World Stress map database release 2008 (*Heidbach et al.* 2008b). Blue symbols indicate thrust faulting (TF), green lines strike-slip faulting (SS) and red lines normal faulting (NF).

Marmara Island. Modelled σ_H orientations near Yalova on Armutlu Peninsula show EW to WNW-ESE orientations in agreement with the WSM data.

At fault segments at which a significant dip-slip component is apparent (from gradients in bathymetry and from the modelled vertical velocity field in figs 5 and 6 of Paper I), σ_H is oriented widely parallel to fault strike for example, at the western part of the Imralı Fault and at the Prince's Islands Segment. This is consistent with σ_H being oriented perpendicular to these basin-bounding faults in opening direction. The accuracy of most of the WSM data in the model area has C-quality (±25°), because the majority comes from single focal mechanism solutions (*Zoback* 1992; *Heidbach et al.* 2010). The mean deviation between the model results and the WSM data is 24.1° (Fig. 4b), therefore slightly less than the accuracy of the data.

3.2 Orientation of principal stresses

Fig. 5(a) shows the modelled σ_1, σ_2 and σ_3 orientations at 5 km depth on a 0.01° × 0.01° grid over the whole model area. The minimum principal stress σ_3 is almost horizontal and trends in NE or SW directions. Both σ_1 and σ_2 either trend NW or SE at shallow or steep plunges. Thus, either of the two principal stresses corresponds to σ_H or σ_V, which is in agreement with the modelled NW-SE orientation of σ_H (Fig. 4a) and the observed transitional stress regime between strike-slip and normal faulting in the Marmara Sea region.

This result is in agreement with principal stress orientations from stress inversions of focal mechanisms (Fig. 5a). Most of the inversion results indicate a strike-slip regime (σ_2 corresponding to σ_V) with a more or less pronounced normal faulting component. The principal stress orientations by *Polat et al.* (2002b) suggest a normal faulting tectonic regime (σ_1 being the steepest principal stress), though also in transition to strike-slip. However, in the western Marmara Sea *Pınar et al.* (2003) found σ_3 to be the steepest principal stress axis and at a similar plunge as σ_2, which means transpression (Fig. 5a). This indicates that local deviations from the prevailing regional stress regime exist. The modelled principal stress orientations shown in Fig. 5(a) agree better with stress inversions that are based on regional data sets than with stress inversions using data from smaller subareas (Fig. 5a, b). The best coincidence is found for the region-wide data sets in which aftershocks are absent and for those comprising major earthquakes (*Gürbüz et al.* 2000; *Polat et al.* 2002a; *Kiratzi* 2002). Aftershocks, which can be controlled by stress perturbations from the main shock (*Gahalaut & Gahalaut* 2008), and stress inversions over small areas can reflect local deviations from the regional stress pattern.

4 STRESS REGIME

4.1 Regime stress ratio (RSR)

To resolve the spatial variations of the modelled stress regime we use the RSR parameter defined by *Simpson* (1997). RSR is basically a combination of the Andersonian faulting type (*Anderson* 1905) represented by the classification index n

$$n = \begin{cases} 0 & \sigma_h < \sigma_H < \sigma_v \quad \text{normal faulting} \\ 1 & \sigma_h < \sigma_v < \sigma_H \quad \text{strike} - \text{slip faulting} \\ 2 & \sigma_v < \sigma_h < \sigma_H \quad \text{thrust faulting} \end{cases} \tag{4}$$

and the ratio of the smaller and greater differential stress (*Bott* 1959)

$$R = \frac{\sigma_2 - \sigma_3}{\sigma_1 - \sigma_3}. \tag{5}$$

RSR is then defined as

$$\text{RSR} = (n + 0.5) + (-1)^n (R - 0.5). \tag{6}$$

An advantageous property of the RSR parameter is that it provides a continuous scale from normal faulting (RSR = 0.5) over strike-slip (RSR = 1.5) to thrust faulting (RSR = 2.5; Fig. 5c). However, as the Andersonian faulting classification is based on Mohr-Coulomb theory the RSR value only describes how an optimally oriented fault would slip. If pre-existing faults are present that are not optimally oriented in the given stress field the type of faulting can deviate from the expected Andersonian type (*Célérier* 1995).

4.2 Overall RSR pattern

Fig. 5(c) shows that most of the Marmara Sea region is in a

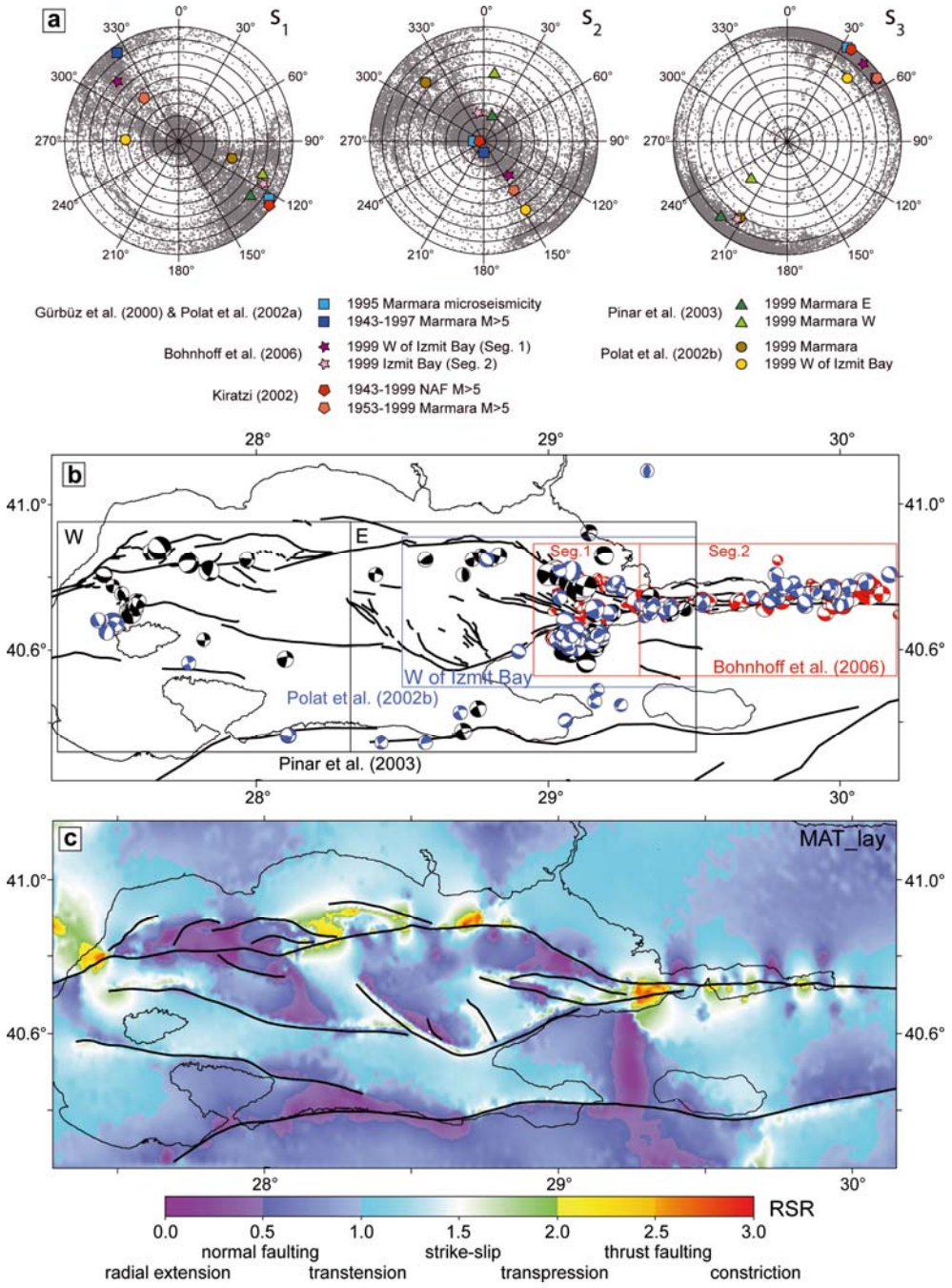

Figure 5. Lower hemisphere stereo plots of principal stress orientations. Grey dots show modelled orientations at 5 km bsl. on a 0.01° × 0.01° grid over the whole model area. Coloured symbols show principal stress orientations from stress tensor inversions of earthquake focal mechanism solutions. (b) Overview map of some of the earthquake focal mechanism data sets used for stress tensor inversion in (a). Mainly aftershocks of the 1999 Izmit earthquake, divided into different subareas, have been used in the studies by *Polat et al.* (2002b), *Pınar et al.* (2003) and *Bohnhoff et al.* (2006). Additional data sets used (not shown in the figure) comprise earthquakes from the whole Marmara Sea region prior to the 1999 event, both from microearthquakes in 1995 and $M > 5$ earthquakes between 1943 and 1997 (*Gürbüz et al.* 2000; *Polat et al.* 2002a; *Kiratzi* 2002). (c) Modelled stress regime at 5 km bsl. in terms of the regime stress ratio RSR.

strike-slip stress regime with some tendency towards a normal faulting stress regime. This result agrees with the general view that the Marmara Sea region is under a strike-slip stress regime characteristic for the North Anatolian Fault throughout most of its length from east Anatolia to the Marmara Sea but in transition to a normal faulting stress regime that prevails in west Anatolia and Greece (*Taymaz et al.* 1991). However, locally deviations from this general stress regime appear as will be discussed thereafter. Furthermore, the results indicate a correlation between stress regime and vertical motion. Areas under prevailing strike-slip or thrust faulting stress regime widely correspond to stable or uplifting areas, whereas areas under a normal faulting stress regime tend to subside (Fig. 5c; fig. 5 of Paper I).

A practical application of the modelled spatial variability in RSR could be the identification of appropriate binning areas for focal mechanisms that are used for stress inversion. This is a key issue as the method of stress inversion requires a priori that all earthquakes used for the inversion are caused by the same stress field (e.g. *Michael* 1984). Further, significant variability of RSR in the proximity of faults indicates that stress can be dominated by the geometry of the fault rather than by the regional stress field, which is particularly important when interpreting data from stress measurements close to faults in a regional context.

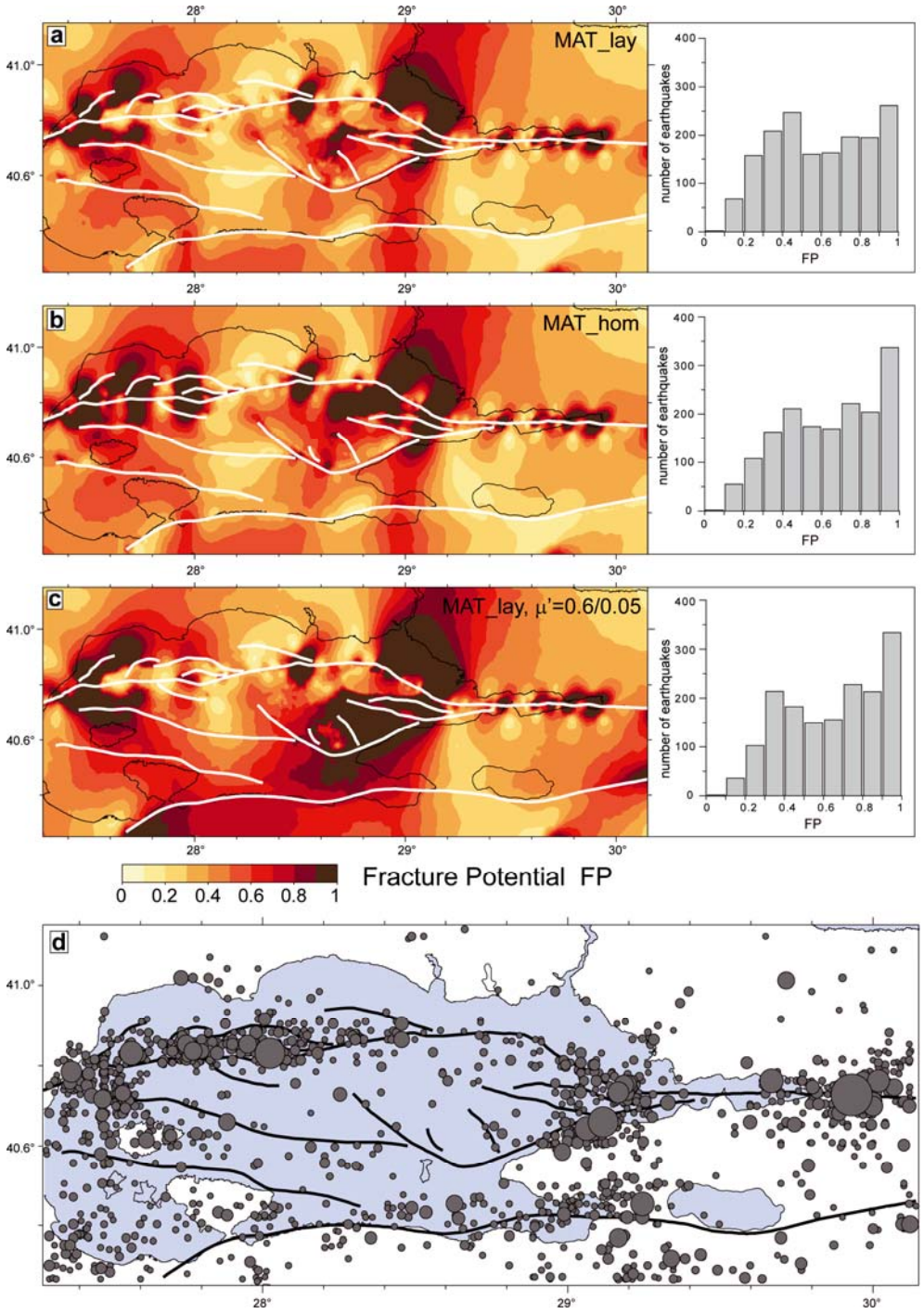

Figure 6. Fracture potential (*FP*) versus seismicity in the Marmara Sea region. (a)-(c) Modelled *FP* at 5 km bsl.; histograms show the distribution of the modelled *FP* values at the location of the $M \geq 3$ earthquakes between 1976 and 2010 from the Kandilli Observatory catalogue without aftershocks of the 1999 Izmit $M = 7.4$ event. (d) Spatial distribution of the $M \geq 3$ earthquakes; circle size is proportional to earthquake magnitude.

4.3 Areas under thrust or normal faulting stress regime

Areas under transpression or thrust faulting stress regime (RSR > 2) are rather small and confined to the neighbourhood of faults. Between the westernmost Izmit Bay and the eastern end of the Çınarcık Basin RSR values > 2 coincide with the location of small thrust faulting earthquakes (*Karabulut et al.* 2002; *Pınar et al.* 2003). Further, a mountain emerging on Hersek Peninsula near a restraining bend of the North Anatolian Fault (*Özaksoy et al.* 2010) and mud volcanoes on the seafloor to the west of Hersek Peninsula (*Cormier et al.* 2006) also indicate transpression. To the west of Istanbul bend transpression is indicated by focal mechanisms with a thrust-faulting component (*Bulut et al.* 2009). Furthermore, the modelled slight transpressional stress regime in the western Marmara Sea between Marmara Island and the Tekirdağ Basin is in agreement with a cluster of strike-slip and thrust faulting focal mechanisms (*Pınar et al.* 2003).

The modelled normal faulting stress regime on Armutlu Peninsula coincides with a prominent cluster of normal faulting focal mechanisms near Yalova (*Karabulut et al.* 2002; *Pınar et al.* 2003). The latter indicate predominant E-W striking fault planes, parallel to the orientation of σ_H (Fig. 4), so that the normal faulting stress regime is associated with N-S extension there.

4.4 Normal faulting stress regime in the Çınarcık Basin but strike-slip motion on the MMF

A normal faulting stress regime is also predicted in the deep basins of the North Marmara Trough (Fig. 5c). This is an apparent contradiction to the strike-slip faulting mechanisms that prevail along the Prince's Islands Segment (*Pınar et al.* 2003; *Bulut et al.* 2009, *Örgülü* 2011). However, the very same model yields almost pure strike-slip motion on the Prince's Islands Segment in agreement with the focal mechanisms (fig. 7 in Paper I). As mentioned in Section 4.1 the type of faulting only reflects the stress regime if the faults are optimally oriented in the stress field. Thus, focal mechanisms on pre-existing non-optimally oriented faults have the potential to reflect the kinematics of slip and the geometry of the fault rather than the stress field (*McKenzie* 1969; *Heidbach et al.* 2010). For instance, slip on a vertical fault will occur in a strikeslip sense even though the stress regime may exhibit components of normal or thrust faulting (e.g. *Célérier* 1995). Moreover, often sets of different fault types altogether represent the associated stress regime in an area rather than a single fault with its specific type of faulting. Such kind of slip partitioning between different faulting types was shown for the San Andreas Fault system and for faults in the Basin and Range (*Jones & Wesnousky* 1992; *Wesnousky & Jones* 1994). In the Marmara Sea strike-slip motion on the MMF is possible despite the normal faulting stress regime because non-vertical secondary faults take up the normal faulting component by dip-slip.

4.5 Influence of rock properties on the modelled stress regime

Comparison of the model in which the sediments are considered (MAT_lay, table 1 in Paper I; Fig. 5c) with a model in which rock properties are distributed homogeneously (MAT_hom; table 1 in Paper I) reveals that the sediments slightly change the stress regime towards normal faulting, for example, under the basins (Fig. S1). Of course, the differences between the inhomogeneous and the homogeneous model are most pronounced in areas in which the basement-topography is below the depth of 5 km bsl. shown here, which mainly concerns the North Marmara Trough (see fig. 2b of Paper I). This means that in the basement below the basins the stress regime is closer to strike-slip than indicated by Fig. 5c. An increase of the coefficient of friction on all faults except the MMF from $\mu' = 0.05$ to 0.6 changes the stress regime from normal faulting and transtension towards strike-slip (Fig. S1b). This change is most pronounced below the Central High, the Imralı Basin, the southern shelf and the southern onshore areas.

5 FRACTURE POTENTIAL

5.1 Differential stress and fracture potential

To visualize how close the modelled stress state is to failure we calculate from the modelled stress tensor the fracture potential (FP) defined by *Connolly & Cosgrove* (1999) as the ratio of the actual differential stress and the critical differential stress at which shear failure occurs

$$FP = \frac{\sigma_d}{\sigma_{d,crit}} = \frac{\sigma_d}{2(C_0 \cos\phi + \sigma_m \sin\phi)}. \quad (7)$$

Here, $\sigma_d = \sigma_1 - \sigma_3$ is the differential stress, σ_1 and σ_3 are the maximum and minimum principal stress, respectively, $\sigma_{d,crit}$ is the critical differential stress at which failure occurs, C_0 is cohesion, σ_m mean stress and ϕ the internal friction angle. The underlying failure criterion is the Mohr-Coulomb criterion. The maximum FP value of one denotes failure, whereas a FP of zero indicates that all three principal stresses are equal. We calculate FP from the modelled differential stress using $\tan\phi = \mu_i = 0.6$ and $C_0 = 30$ MPa, where μ_i is the internal coefficient of friction.

High values of FP are confined to the vicinity of faults, in particular between the Ganos Bend and the Central Basin and in the Çınarcık Basin (Figs 6a-c). In contrast, low values of FP are predicted between the Çınarcık Basin and the Central Basin and on most of the southern shelf. The sediments act to reduce differential stress and FP, which appears from the differences in FP between the inhomogeneous (Figs 6a and c) and the homogeneous model (Fig. 6b). This is because of the sediments' much lower (86 per cent) Young's modulus, which results in lower stress at a given strain. Furthermore, the sediment's lower density compared to the adopted density in the homogeneous model reduces the weight of the overlying rock mass. As a consequence, differential stress and FP

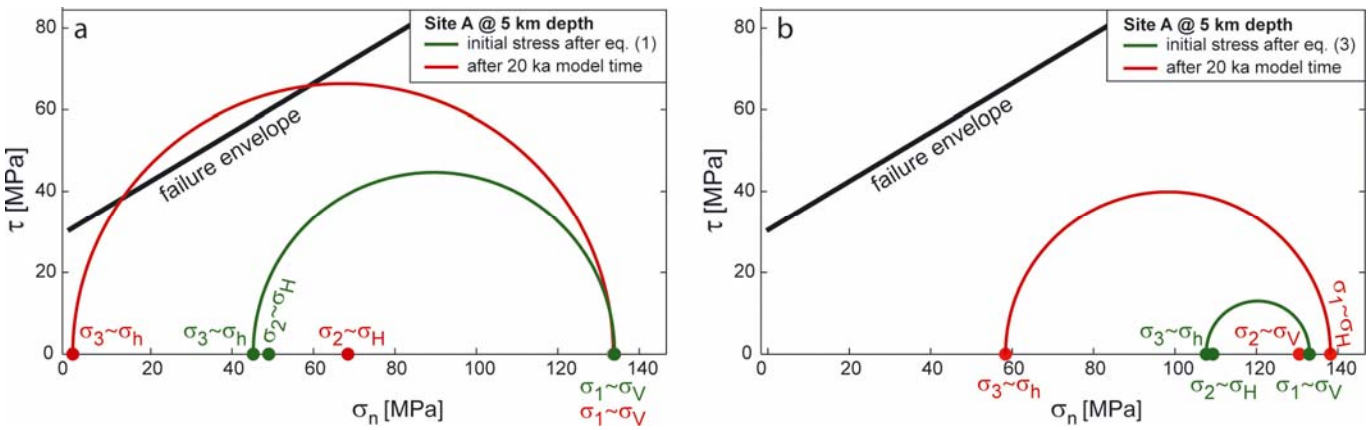

Figure 7. Magnitudes of principal stresses at 5 km bsl. at site 'A' (location given in Fig. 3) from two models using different initial stress state definitions after eqs. (1) and (3). Green circle shows the initial differential stress, red circle the differential stress after application of the kinematic boundary conditions. The black line is the Coulomb-Failure envelope with C_0 = 30 MPa and μ_i = 0.6. Note that consequences of initial stress state for stress regime and FP are substantial (see also Figs S2-S4).

are reduced in the basins because here a normal faulting stress regime ($\sigma_1 = \sigma_V$) prevails (Fig. 5c). In Fig. 6 this *FP*-lowering effect of the sediments is visible only in areas, in which the basement-topography is below the depth of 5 km at which the *FP* results are presented.

Increased friction coefficient of $\mu' = 0.6$ on all faults except the MMF ($\mu' = 0.05$) increases *FP* in particular on Armutlu Peninsula, on the southern shelf and on the southern onshore areas (Fig. 6c). This is because the high friction prevents slip on the fault that follows the southern shore of the Marmara Sea. The slightly extensional boundary conditions at the southern model boundary (P1) then act to reduce σ_h, which is σ_3.

5.2 Fracture potential and seismicity

As fracturing of rock is accompanied by seismicity, we compare the modelled pattern of FP with the observed seismicity distribution (Fig. 6). Though not in detail, the main features of the *FP* pattern are reflected by the seismicity distribution and we find a correlation between *FP* and seismicity in histograms attached to Figs 6(a)-(c). The histograms show the distribution of the modelled *FP* values at the location of the earthquakes.

High *FP* in the western Marmara Sea between the Central Basin and Tekirdağ Basin as well as south of it towards Marmara Island correlates with increased seismicity. The high potential for fracture generation predicted for the eastern Çınarcık Basin and northwestern Armutlu Peninsula is also confirmed by dense seismicity. Low *FP* predicted below the Central High to the east and southeast of the Central Basin correlates with seismicity at a low level. Dense seismicity in the southern part of Armutlu Peninsula, Gemlik Bay and along the southern shore of the Marmara Sea is best explained by the model with high fault friction (Fig. 6).

The probably erroneous patch of high *FP* in the middle of the Central Segment of the MMF is due to a small bend of the MMF in the model that was anticipated from the peculiarities of the mapped surface trace of the MMF there (*Armijo et al.* 2002). Unexpected high *FP* also spreads to the northeast of the Prince's Islands Segment. This is associated with the northern model boundary at which displacements perpendicular to the boundary are not allowed. As a consequence, the prevailing NE-SW extension reduces σ_3 and thus increases differential stress.

5.3 Fault geometry governs fracture potential

From Figs 6(a)-(c) it appears that *FP* is related to fault geometry. The highest differential stresses evolve near strongly curved faults, fault tips or at places where faults come close to each other, for example, between the Central Basin and the Tekirdağ Basin. In contrast, low differential stress and thus low *FP* values characterise areas in which faults are absent or areas surrounding widely straight and vertical fault planes. In particular, the rather straight segment of the MMF between the Istanbul Bend and the Central Basin is characterised by low *FP* values except the mentioned patch in the middle, whereas the MMF exhibits otherwise high *FP* throughout the Marmara Sea. High differential stresses are more or less continuously relieved by microseismicity in the surrounding of these faults. In contrast, plane fault segments do not produce such local peak differential stresses in their surroundings. Therefore, the comparably simple geometry of the Central Segment of the MMF is a possible explanation of the sparseness of earthquakes along it, whereas the complex fault geometries of the adjacent fault segments account for the abundant seismicity in the vicinity of these. Based on this we expect that the Central Segment is capable of accruing high levels of shear stress without reaching critical levels of differential stress, that is, $FP = 1$, in its surrounding.

Our interpretation of the first-order correlation between *FP* and seismicity is that observed seismicity in the Marmara Sea can be widely explained by fracture mechanics based on critical differential stresses that evolve in the surrounding of faults through the interaction between local fault geometries and plate motion.

We would like to point out that *FP* is not directly related to seismic hazard. Large damaging earthquakes normally rupture already existing faults, whereas here the fracturing of intact rock is addressed which is generally associated with earthquakes of smaller magnitude that release local peak differential stresses that accrue in the surrounding of a given fault geometry.

6 INFLUENCE OF INITIAL STRESS ON MODEL RESULTS

To illustrate the impact of the initial stress state on the model results we run a model using eq. (1) instead of eq. (3) to define the reference stress state. Fig. 7 shows the magnitudes of the three principal stresses for both initial stress states prior to and after application of the tectonic boundary conditions at site 'A' located northeast of the Tuzla bend (see Fig. 3) at 5 km depth. Before the tectonic boundary conditions are applied the vertical stress σ_V is the same for both definitions of the initial stress and corresponds to the maximum principal stress σ_1. The two horizontal stresses σ_H and σ_h are roughly equal for either definition of initial stress (small differences at this stage arise from lateral density and stiffness contrasts).

However, the horizontal stresses from the model with initial stress after eq. (3) (Fig. 7b) far exceed the horizontal stresses from the model with initial stress after eq. (1) (Fig. 7a).

6.1 Influence on stress regime and principal stress orientations

After the initial stress is established the subsequent application of the tectonic boundary conditions enlarges the difference between the horizontal stress magnitudes for both definitions of initial stress (Fig. 7). 6h decreases faster than σ_H increases because the tectonic boundary conditions are slightly extensive. However, in the model with initial stress according to eq. (1) a normal faulting stress regime persists (i.e. $\sigma_V > \sigma_H > \sigma_h$) (Fig. 7a and Fig. S2), whereas in the model with initial stress according to eq. (3) a strike-slip regime (i.e. $\sigma_H > \sigma_V > \sigma_h$) evolves as σ_H becomes greater than σ_V (Figs 5 and 7b). The latter case agrees with stress tensor inversions of focal mechanisms, whereas the former case does not. This shows that the choice of the initial stress state has significant impact on the stress regime and the principal stress orientations.

6.2 Influence on fracture potential

Fig. 7 also shows that differential stress after application of tectonic boundary conditions is high and overcritical in the

model with initial stress after eq. (1), whereas differential stress is much smaller and far below the critical value in the model with initial stress after eq. (3). As a consequence, in the former case almost the whole model area exceeds the critical differential stress (Fig. S3), whereas in the latter case critical differential stress emerges only locally and widely agrees with the seismicity distribution (Fig. 6).

Two reasons account for that. First, in the model with initial stress after eq. (1) the horizontal stress magnitudes are much lower than the vertical stress, whereas they are comparable to the vertical stress in the other case (Fig. 7). Secondly, in the model with initial stress after eq. (1) differential stress involves the vertical stress ($\sigma_d = \sigma_1 - \sigma_3 \approx \sigma_V - \sigma_h$), whereas in the other case differential stress is the difference between the two horizontal stresses ($\sigma_d = \sigma_1 - \sigma_3 \approx \sigma_V - \sigma_h$; Fig. 7). In the vicinity of a major transform plate boundary fault such as the North Anatolian Fault shear failure is not expected to arise from differential stresses between σ_V and σ_h. Instead, failure should be due to critical differences between σ_H and σ_h, which arise from the horizontal shear exerted by the relative plate motion, as in the model with initial stress after eq. (3).

6.3 Influence on σ_H orientation and kinematics

Although the principal stress orientations in the models with different initial stress states differ fundamentally from each other, the difference in initial stress state hardly affects σ_H orientation. Deviations in σ_H orientations between the two cases are <5° over most of the model area (Fig. S4). This is due to the fact that in the model with initial stress after eq. (1) σ_H is given by σ_2 whereas in the model with initial stress after eq. (3) σ_H is either σ_1 or σ_2 - while trend is the same. This demonstrates that a model matching observed σ_H orientations does not necessarily represent a meaningful 3-D stress state. Thus, σ_H orientations are not sufficient to constrain the absolute stress state from a geomechanical model.

The difference in velocity between the two models with different initial stress is everywhere less than 1 mm a^{-1}, which is negligible with respect to absolute velocities and which is in the order of the accuracy of GPS measurements. This implies that the different initial stress definitions hardly affect the resulting kinematics and that both models fit the GPS observations equally well.

We conclude that σ_H orientations and kinematic observations can be reproduced by either initial stress definition based on eqs. (1) and (3). However, an appropriate initial stress state is required to predict stress regime, principal stress orientations and differential stresses reliably. A good match of modelled σ_H orientations and kinematics with observations does not imply that the 3-D background stress state of the model is correct.

7 STRESS STATE ALONG THE MMF AND IMPLICATIONS FOR SEISMIC HAZARD

The variable slip rate on the MMF has been interpreted as an indication of segmentation of earthquakes (Paper I; *Hergert & Heidbach* 2010). This is also supported by the normal stress distribution on the MMF. Fault normal stress increases with depth, yet also considerable lateral changes in fault normal stress are revealed (Fig. 8). Normal stress on the Prince's Islands Segment is much lower than on the other segments (Fig. 8). At mid-crustal depths the difference in normal stress between the Prince's Islands Segment and the adjacent fault segments is several hundred MPa or at least a factor of two. Also in the western Marmara Sea below the Tekirdağ Basin fault-normal stress is markedly reduced. These fault sections of reduced normal stress are under a normal faulting stress regime (Fig. 5c). Fault normal stress is greater on the Izmit Segment and on the Central Segment for which a strike-slip regime is predicted. Peak values in normal stress appear near fault bends as on the restraining side of the Ganos Bend, east of the Tuzla Bend and west of the Istanbul Bend. The lateral variations in normal stress are still more expressed for the inhomogeneous rock property distribution that considers the sediments (Fig. 8 bottom) than for the homogeneous model (Fig. 8 top). *Townend & Zoback* (2004) have estimated fault normal stress on the San Andreas Fault at 7.5 km depth to be 180 MPa, which is comparable to our result for the MMF.

The inferred high lateral variations in normal stress along the MMF may considerably affect seismic hazard in the Marmara Sea. Reduced fault normal stress is equivalent to reduced critical shear stress at which frictional resistance is overcome. As a consequence, less shear stress and hence a shorter period of loading is required to exceed the critical shear stress. In this respect, the recurrence rate of earthquakes on the Prince's Islands Segment should be greater (i.e. shorter interevent time) than on the adjacent segments.

Our interpretation of fault segment-wise ruptures of the seismic gap and shorter interevent times for the Prince's Islands Segment is supported by the damage descriptions of historical earthquakes, which were interpreted as that earthquakes have occurred more frequently on the Prince's Islands Segment than on the Central Segment of the MMF (*Ambraseys* 2002). Conversely, the relative rareness of large earthquakes on the Central Segment, which has not ruptured since 1766, may be explained by the highest mean fault normal stress of all MMF segments in the Marmara Sea (Fig. 8). The increase in normal stress towards the Tuzla Bend may have caused the 1999 Izmit earthquake to arrest in the western Izmit Bay, besides the considerable decrease in slip rate between the eastern Izmit Bay and the Tuzla Bend of 3-4 mm a^{-1} (fig. 5a in Paper I). Generally, the marked peaks in fault normal stress for example, at the Ganos Bend, the Istanbul Bend and the Tuzla Bend and the small peaks in the Izmit Bay and Central Basin (Fig. 8) may act as barriers for seismic ruptures. In this respect the modelled normal stress may contribute to localize historical earthquakes and to assess the ends of future ruptures by means of simulation of dynamic rupture propagation.

8 CONCLUSIONS

We presented in this paper the dynamic results of a 3-D geomechanical model of the Marmara Sea region, whose kinematic results are presented in Paper I. Thus, the dynamic (stress state) and the kinematic model results are consistent with the model-independent kinematic and dynamic observations. We modelled the 3-D background stress state and its spatial variability in contrast to relative stresses or stress changes commonly addressed. Our approach to model the background stress state involves an initial stress that hardly affects the kinematics and the σ_H orientations, but strongly influences the orientations and magnitudes of the three prin-

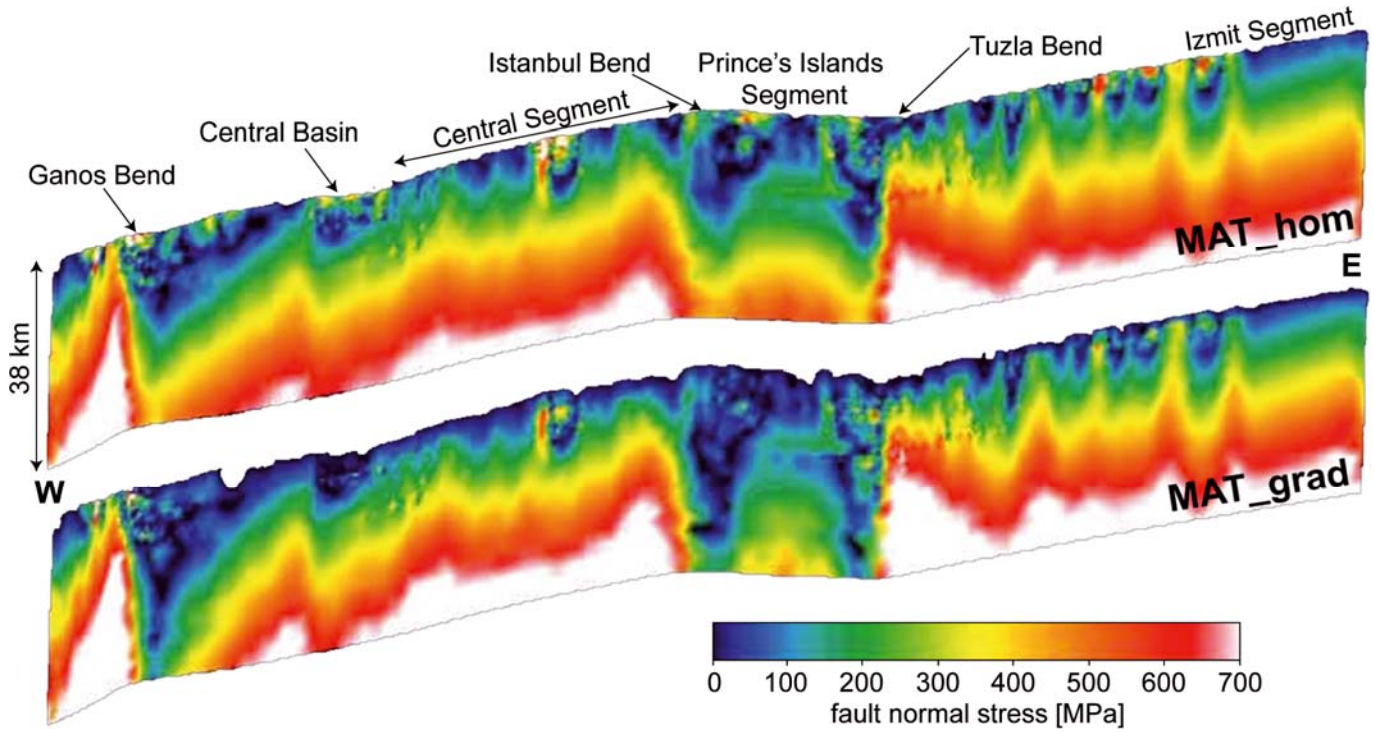

Figure 8. Normal stress on the MMF from models with homogeneous (top; MAT_hom) and inhomogeneous (bottom; MAT_grad) rock properties (see table 1 in Paper I). Note the high lateral contrasts in fault normal stress.

cipal stresses, the stress regime as well as differential stress and fracture potential.

The model widely reproduces available information on the stress state. The distribution and level of off-fault seismicity is governed by fault geometries. Also local variations of the overall NW-SE oriented maximum horizontal stress and of the transtensive stress regime can be referred to fault geometries that perturb the stress field in their surroundings. A direct validation of modelled stress magnitudes by stress measurements is currently not possible because such data at significant depths are not available in the model area.

Normal stress on the MMF undergoes enormous lateral changes in excess of 100 MPa, which makes strain release by a few earthquakes more likely than the occurrence of one large event rupturing the whole seismic gap at once. We draw this conclusion even though the effects of shear stress rate and normal stress on the individual fault segments balance to some extent [e.g. normal stress on the Prince's Islands Segment is lower than on the adjacent fault segments, thereby indicating a shorter interevent time, whereas its lower slip rate indicates a longer interevent time (see Paper I)]. However, despite a likely segmentation of seismic ruptures on the MMF based on both, the modelled kinematics and stress field, the seismic threat to the City of Istanbul is serious, regardless whether the seismic gap will rupture at once or during several less large earthquakes (*Hergert & Heidbach* 2010). In view of the fact that the background stress field can crucially affect rupture propagation (*Oglesby et al.* 2008) the modelled normal stress provides a unique perspective for investigations on the segmentation hypothesis and for simulations of scenario earthquakes by means of rupture propagation modelling.

ACKNOWLEDGMENTS

We thank A. Hirn, B. Müller, K. Fuchs and F. Wenzel for helpful suggestions. We also acknowledge the review of the associated editor Duncan Agnew and two anonymous reviewers. This work was supported by the CEDIM Project at the University of Karlsruhe (TH) and GFZ German Research Centre for Geosciences, the Heidelberg Academy of Sciences and Humanities and the Task Force VII 'Temporal and Spatial Changes of Stress and Strain' of the International Lithosphere Program.

REFERENCES

Ambraseys, N., 2002. The seismic activity of the Marmara Sea Region over the last 2000 years, *Bull. seism. Soc. Am.*, **92**(1), 1-18.

Anderson, E.M., 1905. The dynamics of faulting, *Trans. Edin. Geol. Soc.*, **8**, 387-402.

Armijo, R., Meyer, B., Navarro, S., King, G. & Barka, A., 2002. Asymmetric slip partitioning in the Sea of Marmara pull-apart: a clue to propagation processes of the North Anatolian Fault?, *Terra Nova*, **14**, 80-86.

Bird, P., Ben-Avraham, Z., Schubert, G., Andreoli, M. & Viola, G., 2006. Patterns of stress and strain-rate in southern Africa, *J. geophys. Res.*, **111**, doi:10.1029/2005JB003882.

Bohnhoff, M., Grosser, H. & Dresen, G., 2006. Strain partitioning and stress rotation at the North Anatolian fault zone from aftershock focal mechanisms of the 1999 Izmit M_w = 7.4 earthquake, *Geophys. J. Int.*, **166**, 373-385.

Bott, M.H.P., 1959. The mechanics of oblique slip faulting, *Geol. Mag.*, **96**, 109-117.

Brudy, M., Zoback, M.D., Fuchs, F., Rummel, F. & Baumgärtner, J., 1997. Estimation of the complete stress tensor to 8 km depth in the KTB scientific drill holes: implications for crustal strength, *J. geophys. Res.*, **102**, 18453-18457.

Bulut, F. & Aktar, M., 2007. Accurate relocation of Izmit earthquake (M_w = 7.4, 1999) aftershocks in Çınarcık Basin using Double Difference Method, *Geophys. Res. Lett.*, **34**, L10307, doi:10.1029/2007GL029611.

Bulut, F., Bohnhoff, M., Aktar, M. & Dresen, G., 2007. Characterization of aftershock-fault plane orientations of 1999 Izmit (Turkey) earthquake using high-resolution aftershock locations, *Geophys. Res. Lett.*, **34**, L20306, doi:20310.21029/22007GL031154.

Bulut, F., Bohnhoff, M., Ellsworth, W.L., Aktar, M. & Dresen, G., 2009. Microseismicity at the North Anatolian Fault in the Sea of Marmara offshore Istanbul, NW Turkey, *J. geophys. Res.*, **114**, B09302, doi:

10.1029/2008JB006244.
Carena, S. & Moder, C., 2009. The strength of faults in the crust in the western United States, *Earth planet. Sci. Lett.*, **287**, 373-384.
Célérier, B., 1995. Tectonic regime and slip orientation of reactivated faults, *Geophys. J. Int.*, **121**, 143-161.
Connolly, P. & Cosgrove, J., 1999. Prediction of static and dynamic fluid pathways within and around dilational jogs, in *Fractures, Fluid Flow and Mineralization*, pp. 105-121, McCaffrey, K.J.W., Lonergan, L. & J.J., W., Geological Society, London.
Cormier, M.-H., et al., 2006. North Anatolian Fault in the Gulf of Izmit (Turkey): rapid vertical motion in response to minor bends of a nonvertical continental transform, *J. geophys. Res.*, **111**, doi:10.1029/ 2005JB003633.
Engelder, T. & Fischer, M.P., 1994. Influence of poroelastic behavior on the magnitude of minimum horizontal stress, Sh, in overpressured parts of sedimentary basins, *Geology*, **22**, 949-952.
Eyidoğan, H., 1988. Rates of crustal deformation in western Turkey as deduced from major earthquakes, *Tectonophysics*, **148**, 83-92.
Flesch, L.M., Holt, W.E., Haines, A.J., Wen, L. & Shen-Tu, B., 2007. The dynamics of western North America: stress magnitudes and the relative role of gravitational pontential energy, plate interaction at the boundary and basal tractions, *Geophys. J. Int.*, **169**, 866-896, doi: 10.1111/j.1365. 1246X.2007.03274.x.
Gahalaut, K. & Gahalaut, V.K., 2008. Stress triggering of normal aftershocks due to strike slip earthquakes in compressive regime, *J. Asian Earth Sci.*, **33**, 379-382.
Ghosh, A., Holt, W., Flesch, L.M. & Haines, A.J., 2006. Gravitational potential energy of the Tibetan Plateau and the forces driving the Indian plate, *Geology*, **34**, 321-324, doi:310.1130/G22071.
Gürbüz, C., et al., 2000. The seismotectonics of the Marmara region (Turkey): results from a microseismic experiment, *Tectonophysics*, **316**, 1-17, PII: S0040-1951(0099)00253-X.
Hearn, E.H., McClusky, S., Ergintav, S. & Reilinger, R.E., 2009. Izmit earthquake postseismic deformation and dynamics of the North Anatolian Fault zone, *J. geophys. Res.*, **114**, B08405, doi:10.1029/2008JB006026.
Heidbach, O. & Drewes, H., 2003. 3-D Finite Element model of major tectonic processes in the Eastern Mediterranean, in *New Insights in Structural Interpretation and Modelling*. in Spec. Publ., pp. 259-272, ed. Nieuwland, D., Geol. Soc., London.
Heidbach, O., Reinecker, J., Tingay, M., Müller, B., Sperner, B., Fuchs, K. & Wenzel, F., 2007. Plate boundary forces are not enough: second- and third-order stress patterns highlighted in the World Stress Map database, *Tectonics*, **26**, TC6014, doi:10.1029/2007TC002133.
Heidbach, O., Iaffaldano, G. & Bunge, H.-P., 2008a. Topography growth drives stress rotations in the Central Andes - observations and models, *Geophys. Res. Lett.*, **35**, 8, doi:10.1029/2007GL032782.
Heidbach, O., Tingay, M., Barth, A., Reinecker, J., Kurfeß, D. & Müller, B., 2008b. The World Stress Map database release 2008, doi:10.1594/ GFZ.WSM.Rel2008.
Heidbach, O., Tingay, M., Barth, A., Reinecker, J., Kurfeß, D. & Müller, B., 2010. Global crustal stress pattern based on the World Stress Map database release 2008, *Tectonophysics*, **462**, doi:10.1016/j.tecto. 2009.07.023.
Hergert, T. & Heidbach, O., 2010. Slip-rate variability and distributed deformation in the Main Marmara system, *Nat. Geosci.*, **3**, 132-135, doi:110.1038/NGEO1739.
Hergert, T., Heidbach, O., Bécel, A. & Laigle, M., 2011. Geomechanical model of the Marmara Sea region - I. 3-D contemporary kinematics, *Geophys. J. Int.*, in press, doi:10.1111/1365-246X.2011.04991.x (this issue) (Paper I).
Hickman, S. & Zoback, M.D., 2004. Stress orientations and magnitudes in the SAFOD Pilot Hole, *Geophys. Res. Lett.*, **31**, L15S12, doi:10.1029/ 2004GL020043.
Hubert-Ferrari, A., Barka, A., Jacques, E., Nalbant, S., Meyer, B., Armijo, R., Tapponier, P. & King, G.C.P., 2000. Seismic hazard in the Marmara Sea region following the 17 August 1999 Izmit earthquake, *Nature*, **404**, 269-271.
Humphreys, E.D. & Coblentz, D.D., 2007. North American dynamics and western U.S. tectonics, *Rev. Geophys.*, **45**, doi:10.1029/2005RG000181.
Jaeger, J.C., Cook, N.G.W. & Zimmermann, R.W., 2007. *Fundamentals of Rock Mechanics*, 4th edn, Blackwell Publishing, Oxford.
Jones, C.H. & Wesnousky, S.G., 1992. Variations in strength and slip rate along the San Andreas fault system, *Science*, **256**, 83-86.
Karabulut, H., Bouin, M.-P., Bouchon, M., Dietrich, M., Cornou, C. & Aktar, M., 2002. The seismicity in the Eastern Marmara Sea after the 17 August 1999 İzmit Earthquake, *Bull. seism. Soc. Am.*, **92**, 387-393.
Kiratzi, A.A., 2002. Stress tensor inversions along the westernmost North Anatolian Fault Zone and its continuation into the North Aegean Sea, *Geophys. J. Int.*, **151**, 360-376.
Laigle, M., Bécel, A., de Voogd, B., Hirn, A., Taymaz, T., Özalaybey, S. & Team, S.L., 2008. A first deep seismic survey in the Sea of Marmara: deep basins and whole crust architecture and evolution, *Earth planet. Sci. Lett.*, **270**, 168-179.
Le Pichon, X. & Angelier, J., 1979. The Hellenic arc and trench system: a key to the neotectonic evolution of the eastern Mediterranean area, *Tectonophysics*, **60**, 1-42.
Lorenzo-Martin, F., Roth, F. & Wang, R., 2006. Elastic and inelastic triggering of earthquakes in the North Anatolian Fault zone, *Tectonophysics*, **424**, 271-289.
Lund, B. & Townend, J., 2007. Calculating horizontal stress orientations with full or partial knowledge of the tectonic stress tensor, *Geophys. J. Int.*, **170**, 1328-1335, doi: 10.1111/j.1365-1246X.2007.03468.x.
McGarr, A., 1988. On the state of lithospheric stress in the absence of applied tectonic forces, *J. geophys. Res.*, **93**, 13609-13617.
McKenzie, D., 1969. The relation between fault plane solutions for earthquakes and the directions of the principal stresses, *Bull. seism. Soc. Am.*, **59**, 591-601.
McKenzie, D.P., 1972. Active tectonics of the Mediterranean region, *Geophys. J. R. astr. Soc.*, **30**, 109-185.
Michael, A. J., 1984. Determination of stress from slip data; faults and folds, *J. geophys. Res.*, **89**, 11517-11526.
Müller, B., Wehrle, V., Hettel, S., Sperner, B. & Fuchs, F., 2003. A new method for smoothing oriented data and its application to stress data, in *Fracture and In-situ Stress Characterization of Hydrocarbon Reservoirs*, pp. 107-126, ed. Ameen, M., Geological Society, London.
Muller, J.R., Aydin, A. & Maerten, F., 2003. Investigating the transition between the 1967 Mudurnu Valley and 1999 Izmit earthquakes along the North Anatolian fault with static stress changes, *Geophys. J. Int.*, **154**, 471-482.
Muller, J.R., Aydin, A. & Wright, T.J., 2006. Using an elastic dislocation model to investigate static Coulomb stress change scenarios for earthquake ruptures in the eastern Marmara Sea region, Turkey, in *Analogue and Numerical Modelling of Crustal-Scale Processes*, pp. 397-414, eds. Buiter, S.J.H. & Schreuers, G., Geological Society, London.
Oglesby, D.D., Mai, P.M., Atakan, K. & Pucci, S., 2008. Dynamic models of earthquakes on the North Anatolian fault zone under the Sea of Marmara: Effect of hypocenter location, *Geophys. Res. Lett.*, **35**, doi: 10.1029/ 2008GL035037.
Örgülü, G., 2011. Seismicity and source parameters for small-scale earthquakes along the splays of the North Anatolian Fault (NAF) in the Marmara Sea, *Geophys. J. Int.*, **184**, 385-404, doi:10.1111/ j.1365246X. 2010.04844.x.
Örgülü, G. & Aktar, M., 2001. Regional moment tensor inversion for strong aftershocks of the August 17, 1999 İzmit earthquake (M_w = 7.4), *Geophys. Res. Lett.*, **28**, 371-374.
Özaksoy, V., Emre, Ö., Yıldırım, C., Doğan, A., Özalp, S. & Tokay, F., 2010. Sedimentary record of late Holocene seismicity and uplift of Hersek restraining bend along the North Anatolian Fault, *Tectonophysics*, **487**, 33-45.
Özalaybey, S., Ergin, M., Aktar, M., Tapırdamaz, C., Biçmen, F. & Yörük, A., 2002. The 1999 İzmit earthquake sequence in Turkey: seismological and tectonic aspects, *Bull. seism. Soc. Am.*, **92**, 376-386.
Parsons, T., 2004. Recalculated probability of $M \geq 7$ earthquakes beneath the Sea of Marmara, Turkey, *J. geophys. Res.*, **109**, doi:10.1029/ 2003JB002667.
Parsons, T., Toda, S., Stein, R.S., Barka, A. & Dietrich, J.H., 2000. Heightened odds of large Earthquakes near Istanbul: an interaction-based probability calculation, *Science*, **288**, 661-664.
Pınar, A., Kuge, K. & Honkura, Y., 2003. Moment tensor inversion of recent small to moderate sized earthquakes: implications for seismic hazard and active tectonics beneath the Sea of Marmara, *Geophys. J. Int.*, **153**, 133-145.
Polat, O., et al., 2002a. The Izmit (Kocaeli), Turkey earthquake of 17 August 1999: previous seismicity, aftershocks, and seismotectonics, *Bull. seism. Soc. Am.*, **92**, 361-375.
Polat, O., Eyidogan, H., Haessler, H., Cisternas, A. & Philip, H., 2002b. Analysis and interpretation of the aftershock sequence of the August 17, 1999, Izmit (Turkey) earthquake, *J. Seismol.*, **6**, 287-306.
Provost, A.-S., Chéry, J. & Hassani, R., 2003. 3D mechanical modeling of the GPS velocity field along the North Anatolian fault, *Earth planet. Sci. Lett.*, **209**, 361-377, doi:10.1016/S0012-821X(03)00099-2.
Sato, T., Kasahara, J., Taymaz, T., Ito, M., Kamimura, A., Hayakawa, T. & Tan, O., 2004. A study of microearthquake seismicity and focal mechanisms within the Sea of Marmara (NW Turkey) using ocean bottom seismometers (OBSs), *Tectonophysics*, **391**, 303-314, doi:310.1016/ j.tecto.2004.07.018.
Sheorey, P.R., 1994. A Theory for In Situ Stresses in Isotropic and Transversly Isotropic Rocks, *Int. J. Rock Mech. Min. Sci. Geomech. Abstr.*, 31, 23-34.
Simpson, R.W., 1997. Quantifying Anderson's fault types, *J. geophys. Res.*, **102**, 17909-17919.
Stein, R.S., Barka, A.A. & Dietrich, J.H., 1997. Progressive failure on the

North Anatolian fault since 1939 by earthquake stress triggering, *Geophys. J. Int.*, **128**, 594-604.

Taymaz, T., Jackson, J. & McKenzie, D., 1991. Active tectonics of the north and central Aegean Sea, *Geophys. J. Int.*, **106**, 433-490.

Townend, J. & Zoback, M.D., 2004. Regional tectonic stress near the San Andreas fault in central and southern California. *Geophys. Res. Lett.*, **31**, L15S11, doi:10.1029/2003GL018918.

Wesnousky, S.G. & Jones, C.H., 1994. Oblique slip, slip partitioning, spatial and temporal changes in the regional stress field, and the relative strength of active faults in the Basin and Range, western United States, *Geology*, **22**, 1031-1034.

Zang, A. & Stephansson, O., 2010. *Stress in the Earth's Crust*, 1st edn, 240pp., Springer, Heidelberg.

Zoback, M.L., 1992. First and second order patterns of stress in the lithosphere: the World stress map project, *J. geophys. Res.*, **97**, 11703-11728.

SUPPORTING INFORMATION

Additional Supporting Information may be found in the online version of this article.

The Supporting Information contains the references of the data shown in Fig. 2 and the following supplementary figures:

Figure S1. RSR from the models with homogeneous rock properties and with high friction on the smaller faults.
Figures S2-S4. Stress results from the model with initial stress after eq. (1) instead of eq. (3).

Please note: Wiley-Blackwell are not responsible for the content or functionality of any supporting materials supplied by the authors. Any queries (other than missing material) should be directed to the corresponding author for the article.